PHYSICAL REVIEW A **89**, 023416 (2014)

Pathway dynamics in the optimal quantum control of rubidium: Cooperation and competition

Fang Gao,[1] Roberto Rey-de-Castro,[2] Ashley M. Donovan,[2] Jian Xu,[3] Yaoxiong Wang,[1] Herschel Rabitz,[2,*] and Feng Shuang[1,†]
[1]*Institute of Intelligent Machines, Chinese Academy of Sciences, Hefei 230031, China*
[2]*Department of Chemistry, Princeton University, Princeton, New Jersey 08544, USA*
[3]*Department of Chemistry, Nankai University, Tianjin 300071, China*

(Received 10 December 2013; published 13 February 2014)

The dynamics that take place in the optimal quantum control of atomic rubidium upon population transfer from state $5S_{1/2}$ to state $5D_{3/2}$ are investigated with Hamiltonian-encoding–observable-decoding (HE-OD). For modest laser powers two second-order pathways, $5S_{1/2} \rightarrow 5P_{3/2} \rightarrow 5D_{3/2}$ (pathway 1) and $5S_{1/2} \rightarrow 5P_{1/2} \rightarrow 5D_{3/2}$ (pathway 2), govern the population transfer process. Pathway 1 has larger transition dipoles than pathway 2. However, state $5P_{3/2}$ along pathway 1 may also be excited to an undesired state $5D_{5/2}$, which can result in population "leakage." Thus, the two pathways may either cooperate or compete with each other in various dynamical regimes. An important feature in the case of cooperation is that the ratio between the amplitudes of pathways 1 and 2 oscillates over time with a frequency equal to the detuning between transitions $5S_{1/2} \rightarrow 5P_{3/2}$ and $5P_{3/2} \rightarrow 5D_{3/2}$. We also study the regime in which pathway 2 dominates the dynamics when the larger transition dipoles of pathway 1 can no longer compensate for its population leakage. The overall analysis illustrates the utility of HE-OD as a tool to reveal the quantum control mechanism.

DOI: 10.1103/PhysRevA.89.023416 PACS number(s): 32.80.Qk, 02.70.−c

I. INTRODUCTION

The control of quantum dynamics has many potential applications and various techniques have been proposed to achieve control [1]. One of the most widely used strategies in the laboratory is adaptive feedback control (AFC) [2–11], in which a learning algorithm [12] is employed to guide laser experiments in the search for optimal control fields [13–19]. In many cases, the optimal control may be complex making it a challenge to gain an understanding of the underlying mechanism [20,21]. To reveal the mechanism, modeling is often done possibly with the aid of additional experiments. The Hamiltonian-encoding–observable-decoding (HE-OD) technique [22–26] provides a protocol for direct laboratory investigation of the mechanism induced by the laser field [27–29]. Importantly, HE-OD often can be implemented with only software changes guiding the laser apparatus of many AFC experiments. HE-OD yields the control mechanism expressed in the form of the amplitudes and phases for the various quantum pathways connecting the target and initial states. Here a pathway is specified by a sequence of transitions $|a\rangle \rightarrow |l_1\rangle \rightarrow |l_2\rangle \rightarrow \cdots \rightarrow |l_{n-1}\rangle \rightarrow |b\rangle$, where the states $|l_i\rangle$, $i = 1,2,\ldots,n-1$, prescribe one particular path of n steps from the initial state $|a\rangle$ to the target state $|b\rangle$. The flexibility inherent in HE-OD permits utilizing and manipulating the pathways in various ways by maximizing an appropriate objective function. Since its first laboratory implementation [27], HE-OD has been applied to pathway control [28] and time-resolved pathway amplitude reconstruction [29] in atomic Rb. These experiments have demonstrated HE-OD's potential as a tool for mechanism analysis as well for using mechanism information to guide the quantum control process. In the present work, the pathway dynamics in the optimal control of atomic Rb are theoretically studied and the underlying dynamics are analyzed.

The paper is organized as follows. Section II gives a brief description of the HE-OD simulation procedure. In Sec. III HE-OD is applied to the simulated quantum control of atomic Rb. For modest laser powers, two second-order pathways dominate in the dynamics. Two field regimes are analyzed to study the cooperation and competition between pathways. As also observed in the laboratory [29], oscillations appear in the time evolution of ratio of the magnitudes of the pathway amplitudes, even though the laboratory field was qualitatively distinct. Section IV provides an analytical explanation for the oscillations in the amplitude ratios when pathways 1 and 2 are of the same importance under the considered simulated laser bandwidth. Concluding remarks are given in Sec. V.

II. HE-OD PROCEDURE

The Hamiltonian of atomic Rb is of the form $H = H_0 - \mu E(t)$, where H_0 is the unperturbed Hamiltonian with eigenstates $|l_p\rangle$, $p = 1,2,\ldots,5$, and μ is the dipole moment operator. The energy level structure is shown in Fig. 1. In the basis $\{|l_p\rangle\}$, $p = 1,2,\ldots,5$, the matrices H_0 and μ are given by

$$H_0 = \begin{bmatrix} 0 & 0 & 0 & 0 & 0 \\ 0 & \omega_1 & 0 & 0 & 0 \\ 0 & 0 & \omega_2 & 0 & 0 \\ 0 & 0 & 0 & \omega_1+\omega_3 & 0 \\ 0 & 0 & 0 & 0 & \omega_1+\omega_3 \end{bmatrix},$$

$$\mu = \begin{bmatrix} 0 & \mu_{12} & \mu_{13} & 0 & 0 \\ \mu_{12} & 0 & 0 & \mu_{24} & \mu_{25} \\ \mu_{13} & 0 & 0 & \mu_{34} & 0 \\ 0 & \mu_{24} & \mu_{34} & 0 & 0 \\ 0 & \mu_{25} & 0 & 0 & 0 \end{bmatrix}, \quad (1)$$

where the energy of state $|1\rangle$ is set to zero, levels $|4\rangle$ and $|5\rangle$ are degenerate, $\omega_1 + \omega_3 = \omega_2 + \omega_4 = 0.1171$, $\omega_1 = 0.058\,40$, $\omega_2 = 0.057\,31$, $\mu_{12} = 4.2275$, $\mu_{13} = 2.9931$, $\mu_{24} = 1.0216$, $\mu_{25} = 1.0238$, and $\mu_{34} = 0.9$ [30,31]. Unless other-

---

[*] hrabitz@princeton.edu

[†] shuangfeng@ustc.edu.cn

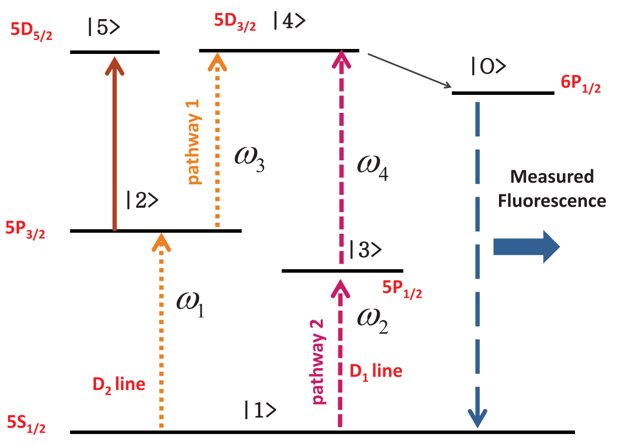

FIG. 1. (Color online) The energy level structure of atomic Rb. Here states $|1\rangle$, $|2\rangle$, $|3\rangle$, $|4\rangle$, $|5\rangle$, and $|O\rangle$ denote the $5S_{1/2}$, $5P_{3/2}$, $5P_{1/2}$, $5D_{3/2}$, $5D_{5/2}$, and $6P_{1/2}$ levels, respectively. The transitions $|1\rangle \to |2\rangle, |1\rangle \to |3\rangle, |2\rangle \to |4\rangle, |2\rangle \to |5\rangle$, and $|3\rangle \to |4\rangle$ are dipole allowed. In the laboratory, state $|4\rangle$ will decay to $|O\rangle$, and thus the population of the target state $|4\rangle$ is proportional to the measured fluorescence emitted from $|O\rangle$.

wise noted, the energies and dipole matrix elements in this paper are given in atomic units

The dynamics in the Schrödinger representation are described by

$$i\frac{dU(t)}{dt} = [H_0 - \mu E(t)]U(t), \tag{2}$$

where U is the evolution operator. In the interaction representation, the Hamiltonian reduces to $V_I(t) = -\exp(-iH_0t)\mu E(t)\exp(iH_0t)$, and the equation of motion becomes

$$i\frac{dU_I(t)}{dt} = V_I(t)U_I(t). \tag{3}$$

The solution of Eq. (3) can be expressed in terms of the Dyson expansion

$$U_I(t) = I + (-i)\int_0^t V_I(t_1)dt_1 + (-i)^2\int_0^t V_I(t_2)\int_0^{t_2} V_I(t_1)dt_1dt_2 + \cdots . \tag{4}$$

Denoting the initial state as $|a\rangle$ and the final state as $|b\rangle$ at time t, then the transition amplitude is given by $\langle b|U_I(t)|a\rangle$, which can be expanded in terms of quantum pathway amplitudes,

$$\langle b|U_I(t)|a\rangle = \sum_{n,\{l_p\}} U_{ba}^{n(l_1,l_2,\ldots,l_{n-1})}(t) \tag{5}$$

with

$$\sum_{n,\{l_p\}} U_{ba}^{n(l_1,l_2,\ldots,l_{n-1})}(t) = (-i)^n \sum_{\{l_p\}} \int_0^t \langle b|V_I(t_n)|l_{n-1}\rangle \int_0^{t_n} \langle l_{n-1}|V_I(t_n)|l_{n-2}\rangle \times \cdots \int_0^{t_2} \langle l_1|V_I(t_1)|a\rangle\, dt_1 \cdots dt_{n-1}dt_n. \tag{6}$$

The pathway amplitude $U_{ba}^{n(l_1,l_2,\ldots,l_{n-1})}(t)$ corresponds to a transition from $|a\rangle$ to $|b\rangle$ through the sequence of n steps $|a\rangle \to |l_1\rangle \to |l_2\rangle \to \cdots \to |l_{n-1}\rangle \to |b\rangle$, which constitutes one of the nth-order pathways linking $|a\rangle$ and $|b\rangle$. Here $|a\rangle$, $|b\rangle$, and $\{|l_p\rangle\}$ are all eigenstates of H_0; the same analysis holds for other bases, and a different choice of intermediate state $\{|l_p\rangle\}$ will give a new specification of quantum pathways to possibly provide additional insights into the mechanism [22,23].

The HE-OD methodology consists of encoding the Hamiltonian such that each pathway amplitude of interest has a unique signature in the output signal. In an experimental implementation, encoding may be conveniently done with respect to the field's spectral phases through the use of a standard laser pulse shaper [27–29], while in simulations the Hamiltonian can be encoded more flexibly [24]. The HE-OD procedure employed in this work entails a sequence of (simulations) experiments with different encodings. At the sth experiment, in general, each element of matrix V_I may be modulated with the encoding function $m_{pq}(s)$ such that

$$(V_I)_{pq} \to (V_I)_{pq}\, m_{pq}(s). \tag{7}$$

Then Eq. (3) becomes

$$i\frac{dU_I(t,s)}{dt} = \begin{pmatrix} [V_I(t)]_{11}m_{11}(s) & \cdots & [V_I(t)]_{1d}m_{1d}(s) \\ \vdots & \vdots & \vdots \\ [V_I(t)]_{d1}m_{d1}(s) & \cdots & [V_I(t)]_{dd}m_{dd}(s) \end{pmatrix} U_I(t,s), \tag{8}$$

whose solution is

$$\langle b|U_I(t,s)|a\rangle = \sum_{n,\{l_p\}} U_{ba}^{n(l_1,l_2,\ldots,l_{n-1})}(t) M_{ba}^{n(l_1,l_2,\ldots,l_{n-1})}(s) \tag{9}$$

with

$$M_{ba}^{n(l_1,l_2,\ldots,l_{n-1})}(s) = m_{bl_{n-1}}(s)m_{l_{n-1}l_{n-2}}(s)\ldots m_{l_1a}(s). \tag{10}$$

It is possible to design the encoding functions $\{m_{pq}(s)\}$ such that $M_{ba}^{n(l_1,l_2,\ldots,l_{n-1})}(s)$ only depends on n, regardless of the sequence of intermediate state $\{|l_p\rangle\}$. In this case we have

$$\begin{aligned}\langle b|U_I(t,s)|a\rangle &= \sum_{n,\{l_p\}} U_{ba}^{n(l_1,l_2,\ldots,l_{n-1})}(t) M_{ba}^{n(l_1,l_2,\ldots,l_{n-1})}(s) \\ &= \sum_n M_{ba}^n(s) \sum_{\{l_p\}} U_{ba}^{n(l_1,l_2,\ldots,l_{n-1})}(t) \\ &= \sum_n M_{ba}^n(s) U_{ba}^n(t). \end{aligned} \tag{11}$$

Thus, in our simulations, the control mechanism is expressed in terms of two types of quantum pathways. The first case is associated with Eq. (9) where detailed intermediate states are revealed through the extraction of $U_{ba}^{n(l_1,l_2,\ldots,l_{n-1})}$. The second case focuses on the overall amplitude $U_{ba}^n(t)$ at order n extracted from Eq. (11).

For the objective of detailed pathway identification, the encoding function is chosen as $m_{pq}(s) = \exp(2\pi i\gamma_{pq}s/N)$, where N is the number of simulations performed (i.e.,

$s = 1,2,\ldots,N$), and the frequencies γ_{pq} are picked to make the identification functions $M_{ba}^{n(l_1,l_2,\ldots,l_{n-1})}$ orthogonal and unique for the investigated type of pathways. In this case, $M_{ba}^{n(l_1,l_2,\ldots,l_{n-1})}(s) = \exp(2\pi i \gamma_{n(l_1,l_2,\ldots,l_{n-1})} s/N)$, where $\gamma_{n(l_1,l_2,\ldots,l_{n-1})} = \gamma_{bl_{n-1}} + \gamma_{l_{n-1}l_{n-2}} + \ldots \gamma_{l_1 a}$. All $\{\gamma_{pq}\}$ are taken to be positive integers such that we can have a unique value of $\gamma_{n(l_1,l_2,\ldots,l_{n-1})}$ for each investigated specific pathway. For the objective of considering the contributing pathway orders, all $\{\gamma_{pq}\}$ are equal to 1, so that the identification function is $M_{ba}^{n}(s) = \exp(2\pi i \gamma_n s/N)$, where $\gamma_n = n$. It is easy to see that

$$\frac{1}{N}\sum_{s=1}^{N} M_{ba}^{n(l_1,l_2,\ldots,l_{n-1})}(s)^* M_{ba}^{n'(l'_1,l'_2,\ldots,l'_{n-1})}(s) = \delta_{n(l_1,l_2,\ldots,l_{n-1}),n'(l'_1,l'_2,\ldots,l'_{n-1})}, \quad (12)$$

$$\frac{1}{N}\sum_{s=1}^{N} M_{ba}^{n}(s)^* M_{ba}^{n'}(s) = \delta_{n,n'}. \quad (13)$$

Due to the above orthogonality relationships, the amplitudes $U_{ba}^{n(l_1,l_2,\ldots,l_{n-1})}$ and U_{ba}^{n} can be computed by the inverse fast Fourier transform (IFFT) of their corresponding modulated matrix element $U_{ba}(s)$ along with knowledge of the particular frequencies $\gamma_{n(l_1,l_2,\ldots,l_{n-1})}$ and γ_n, respectively. In practice, HE-OD is performed by solving Eq. (8) N times with chosen encoding functions followed by application of the IFFT operation.

III. PATHWAY DYNAMICS IN ATOMIC RUBIDIUM

A. Simulation details

In this section, HE-OD is employed to study pathway dynamics in atomic Rb. The electric field $E(t)$ in Eq. (2) is assumed to be of the form

$$E(t) = \exp[-(t - t_{1/2})^2/\Delta^2] \sum_{k=1}^{4} A_k \cos(\omega_k t + \varphi_k), \quad (14)$$

where the target time $T = 4$ ps, $t_{1/2} = 2$ ps, and $\Delta = (1\text{ ps})/\sqrt{\ln 2}$. Thus, the field corresponds to a pulse with a temporal full width at half maximum (FWHM) of 2 ps. In the simulations, eight parameters (A_1, A_2, A_3, A_4, φ_1, φ_2, φ_3, φ_4) are optimized to maximize population transfer $P_{41} = |\langle 4\,|U(T,0)|\,1\rangle|^2$ from the initial state $|1\rangle$ to the target state $|4\rangle$ at final time T. A genetic algorithm (GA) is employed to obtain the field that maximizes P_{41}.

A minimum of two resonant photons are needed to induce the transition from state$|1\rangle$ to state $|4\rangle$ following pathways 1 or 2 in Fig. 1. The corresponding two lowest-order Dyson expansion terms U_1 and U_2 are given by

$$U_1 = \mu_{12}\mu_{24}\int_0^T e^{-i\omega_3 t_2} E(t_2) \int_0^{t_2} e^{-i\omega_1 t_1} E(t_1) dt_1 dt_2, \quad (15)$$

$$U_2 = \mu_{13}\mu_{34}\int_0^T e^{-i\omega_4 t_2} E(t_2) \int_0^{t_2} e^{-i\omega_2 t_1} E(t_1) dt_1 dt_2. \quad (16)$$

Upon obtaining an optimal field, two encoding matrices for $\{\gamma_{pq}\}$, denoted as γ_I and γ_{II}, are adopted to extract the two types of pathway amplitudes $U_{ba}^{n(l_1,l_2,\ldots,l_{n-1})}$ and U_{ba}^{n}, respectively, discussed in Sec. II:

$$\gamma_I = \begin{pmatrix} 0 & 1 & 5 & 0 & 0 \\ 1 & 0 & 0 & 23 & 97 \\ 5 & 0 & 0 & 379 & 0 \\ 0 & 23 & 379 & 0 & 0 \\ 0 & 97 & 0 & 0 & 0 \end{pmatrix},$$

$$\gamma_{II} = \begin{pmatrix} 0 & 1 & 1 & 0 & 0 \\ 1 & 0 & 0 & 1 & 1 \\ 1 & 0 & 0 & 1 & 0 \\ 0 & 1 & 1 & 0 & 0 \\ 0 & 1 & 0 & 0 & 0 \end{pmatrix}. \quad (17)$$

With the encoding matrix γ_I, the amplitudes U_1 and U_2, respectively, of pathway 1 ($|1\rangle \to |2\rangle \to |4\rangle$) and pathway 2 ($|1\rangle \to |3\rangle \to |4\rangle$), can be extracted from the IFFT of the amplitude $U_{41}(s)$ at frequencies 24 and 384, respectively, while with the encoding matrix γ_{II}, the frequency is n for each nth-order pathway. In both cases, $N = 1600$ steps in s were used in the HE-OD calculations.

In the following subsection, we will analyze the dynamics induced by fields that optimize the $|1\rangle \to |4\rangle$ population transfer. The optimizations were carried out by imposing different sets of constraints on the four optimization parameters of A_1, A_2, A_3, and A_4.

B. Fighting for the dominant role

In the weak-field regime, pathways 1 and 2 are the two lowest-order routes connecting the initial state $|1\rangle$ and the target state $|4\rangle$. As evident in Fig. 1 and the transition dipole matrix in Eq. (1), the intermediate state $|2\rangle$ is also coupled to state $|5\rangle$, while the intermediate state $|3\rangle$ is only coupled to the higher target state $|4\rangle$. Importantly, to reach the target state $|4\rangle$ through state $|5\rangle$ minimally calls for the fourth-order pathway $|1\rangle \to |2\rangle \to |5\rangle \to |2\rangle \to |4\rangle$, or even higher order. At weak fields, possible "leakage" of amplitude to state $|5\rangle$ should not affect the population dynamics leading to the target state $|4\rangle$. The possible consideration of leakage (i.e., loss of final maximum amplitude in state $|4\rangle$) arises due to a special circumstance for Rb where $\mu_{42} \approx \mu_{52}$ and $\omega_{42} = \omega_{52}$. Thus, the system is likely not fully controllable to a practical degree, as it can be difficult to simultaneously manage the dynamics leading to the transitions $|2\rangle \to |4\rangle$ and $|2\rangle \to |5\rangle$. If the effect of the leakage is large, the optimization algorithm may choose to reach the target state $|4\rangle$ through state $|3\rangle$ just along pathway 2 instead of through state $|2\rangle$. Balancing the possibility of leakage to state $|5\rangle$, pathway 1 has the advantage of μ_{12} being considerably larger than μ_{13} of pathway 2. These effects can induce cooperation and/or competition between the two pathways in various circumstances. It will be shown that for strong fields a fourth-order pathway has a contribution that cannot be ignored. The numerical simulations will demonstrate the cooperation and competition between pathways 1 and 2. To treat the weak-field regime the four spectral amplitudes A_1, A_2, A_3, and A_4 were constrained to have a small upper limit. In this case, the spectral amplitudes of the optimal field along pathway 1 (A_1, A_3) and pathway 2 (A_2, A_4) were found to approximately have the same magnitude. Therefore, in the weak-field regime the two pathways cooperate with each other to maximize the population transfer. For example, when the four amplitude

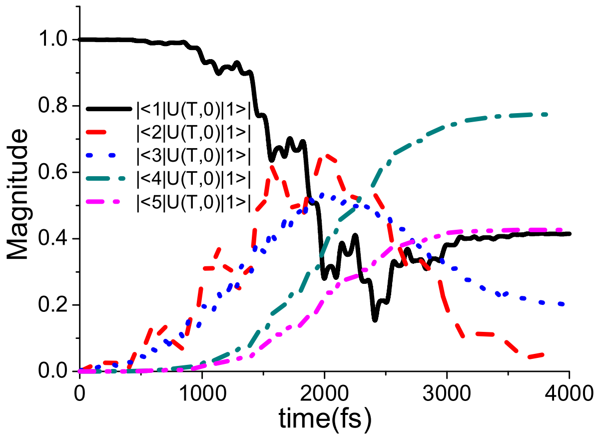

FIG. 2. (Color online) The control field driven dynamics for the magnitude of the amplitudes for all five states of atomic Rb expressed as $|\langle j\,|U(T,0)|\,1\rangle|$, $j = 1,\ldots,5$. The population of a state is the square of its amplitude. The control field is optimized with amplitudes A_k in Eq. (12) being limited in the range $[0, 2.5 \times 10^{-5}]$. Cooperation between two pathways is observed in this case.

parameters are restricted to the range $[0, 2.5 \times 10^{-5}]$, the optimal result is $A_1 = 1.054 \times 10^{-5}$, $A_2 = 1.169 \times 10^{-5}$, $A_3 = 2.486 \times 10^{-5}$, $A_4 = 2.483 \times 10^{-5}$. The corresponding peak intensity of the laser field is about 0.004 V/Å. The high resolution used here for the field parameters is generally not required in the experiments; for an assessment of the necessary field resolution see the discussion on the encoding functions in Refs. [28,29]. The population dynamics under the optimal laser field are shown in Fig. 2. The final transition probability to the target state was $|\langle 4\,|U(T,0)|\,1\rangle|^2 = 0.602$, and Fig. 2 shows that the population in state $|4\rangle$ increases monotonically with time.

The similar value of A_1 and A_2 (also A_3 and A_4) indicates that the magnitudes of amplitudes for pathway 1 ($|U_1|$) and pathway 2 ($|U_2|$) should be similar, which is consistent with the nearly same population dynamics of states $|2\rangle$ and $|3\rangle$ in Fig. 2. The HE-OD extracted amplitudes of the different pathways are extracted at T as listed in Tables I and II. The tables show that, due to the weak nature of the laser field, the second-order pathways have the largest amplitude. Pathways 1 and 2 have almost the same phase, and their amplitudes in Table II add up to give ∼1.790, very close to the value of 1.7830 in Table I, which indicates their constructive interference and cooperation [see also Fig. 3(a)] [24].

TABLE I. Significant pathway orders for the control field driven dynamics in Fig. 2.

Order	Amplitude	Phase
2	1.7830	1.7857
4	1.3233	−1.2882
6	0.3473	1.9297
8	0.03260	−1.0485

TABLE II. Amplitudes and phases of significant 2nd- and 4th-order quantum pathways for the control field driven dynamics in Fig. 2.

Pathway	Amplitude	Phase
(1 → 2 → 4) (Pathway 1)	1.0551	1.7125
(1 → 3 → 4) (Pathway 2)	0.7349	1.8909
(1 → 2 → 1 → 2 → 4)	0.3336	−1.5608
(1 → 2 → 1 → 3 → 4)	0.2563	−0.7793
(1 → 3 → 1 → 2 → 4)	0.2105	−1.3505
(1 → 3 → 1 → 3 → 4)	0.1413	−1.2748
(1 → 2 → 5 → 2 → 4)	0.1073	−1.3992
(1 → 2 → 4 → 2 → 4)	0.1068	−1.3992
(1 → 2 → 4 → 3 → 4)	0.08256	−1.3633
(1 → 3 → 4 → 2 → 4)	0.07436	−1.2456
(1 → 3 → 4 → 3 → 4)	0.05751	−1.2376

For stronger fields (i.e., the upper limit of four amplitude parameters is higher), the larger transition dipoles in pathway 1 are not sufficient to manage the population leakage to state $|5\rangle$ along this route. Thus, the field amplitudes along pathway 2 (A_2, A_4) tend to have much larger values than those along pathway 1 (A_1, A_3). For example, allowing the four amplitude parameters to lie in the range $\left[0, 4 \times 10^{-5}\right]$, then the optimal result is $A_1 = 3.872 \times 10^{-6}$, $A_2 = 1.755 \times 10^{-5}$, $A_3 = 1.301 \times 10^{-5}$, and $A_4 = 3.989 \times 10^{-5}$. With the same peak intensity essentially as before (0.004 V/Å) the control mechanism is different with pathway 2 dominating the dynamics. The dynamics under the optimal laser field are shown in Fig. 4. The population leakage to state $|5\rangle$ is about 0.01 because the algorithm chose a field that avoided pathway 1. The final transition probability to the target state is $|\langle 4\,|U(T,0)|\,1\rangle|^2 = 0.822$. Figure 4 shows that the magnitude of the transition amplitude in intermediate state $|3\rangle$ in pathway 2 is much larger than that of the intermediate state $|2\rangle$ in pathway 1. Table III shows that the second-order pathways also have the largest amplitude. Table IV shows that pathway 2 contributes almost 90% to the second-order amplitude, and the similar phases indicate cooperation between the two pathway amplitudes [see also Fig. 3(b)]. The fourth-order pathways in Table IV also have significant amplitude, and are mostly through state $|3\rangle$ instead of state $|2\rangle$, while the two intermediate states show equal importance in Table II.

In the two cases above, the second-order pathways dominate for fields of modest amplitude. For even stronger fields, higher order processes become much more important as shown in Fig. 5. The fields E_1 and E_2 are the two cases in Figs. 2 and 4, respectively. There is no significant qualitative difference in pathway order distribution for E_1 and E_2, although the specific pathways involved are different. When the peak field amplitude increases to ∼0.01 V/Å (E_3), higher order (beyond fourth-order) pathways have very significant contributions with the second-order pathways no longer being dominant.

The dynamics is also plotted for the three cases in Fig. 5. It is found that the magnitude of the transition amplitude for the target state oscillates for E_3, while it increases monotonically with time for E_1 and E_2. This difference reflects the higher order processes involved with E_3, producing Rabi oscillations. In these simulations, a perfect yield is not attained, which is likely due to the following reasons. First, the system is difficult to be fully controlled. As shown in Eq. (1), the energy

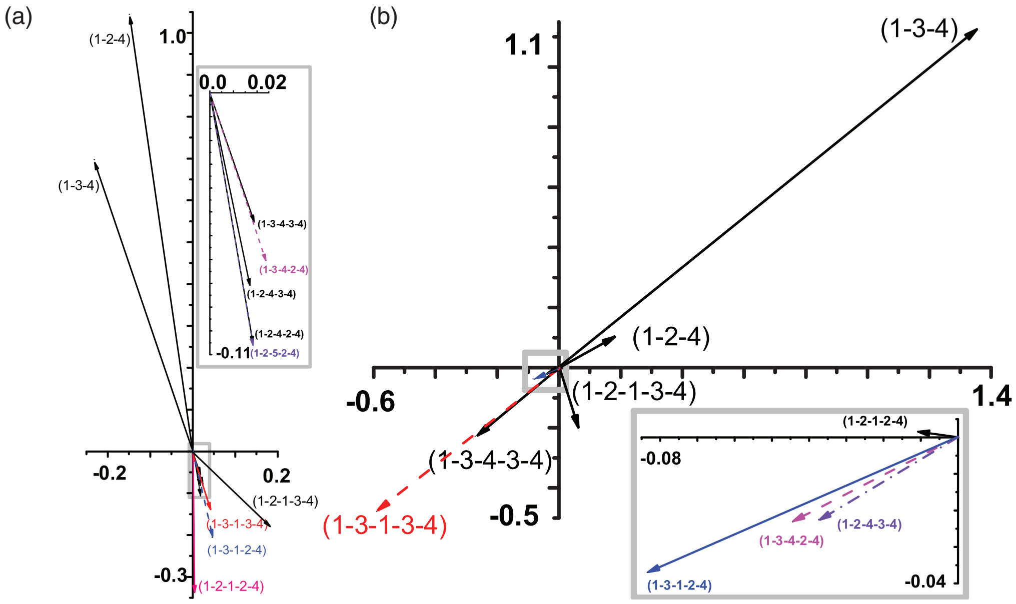

FIG. 3. (Color online) (a), (b) The complex plane representations of the pathway amplitudes in Tables II and IV, respectively. The insets in (a) and (b) show the magnification of the quantum pathways in their corresponding light gray boxes.

levels $|4\rangle$ and $|5\rangle$ are degenerate, and the corresponding two transition dipole moments from the intermediate state $|2\rangle$, μ_{42} and μ_{52}, have very similar values. This makes it difficult to simultaneously manage the dynamics involving the transitions $|2\rangle \rightarrow |4\rangle$ and $|2\rangle \rightarrow |5\rangle$. Second, the controls are restricted to an on-resonance condition, the duration is fixed at ~4 ps, and the field amplitudes are constrained to modest values.

IV. RATIO OF TWO PATHWAY AMPLITUDES

Experimentally it is convenient to measure the ratios of pathway amplitudes instead of absolute values of the amplitudes themselves. Thus, here we focus on ratios by calculating time-resolved pathway ratios for different dynamical scenarios. The pathway ratios contain rich information about the dynamics of the population transfer process. Time-resolved quantum process tomography has been experimentally demonstrated using HE-OD [29] in the weak-field regime by combining HE-OD with a laser pulse truncation procedure, and one important observed feature was the oscillation of the ratio $|U_1/U_2|$. In this section, we will show that this behavior also appears for the low-bandwidth pulses considered here and explained in terms of a simple analytical physical model.

In the experiment [29], the encoded field truncated at time τ, $E_s(t,\tau)$, was generated by cutting off the encoded field $E_s(t)$ for $t > \tau$ with the use of an appropriate spatial light modulator mask. Then by decoding the modulated observables $O_s(\tau)$ (fluorescence) as a function of s, the time-resolved dynamics were resolved from the pathway amplitudes as a function of τ. In simulations, we first truncated the laser field $E(t)$ to be zero for $t > \tau$ and then performed a HE-OD analysis, which is equivalent to the experimental procedure.

The dynamics for the two pathways corresponding to the first two cases (modest laser powers) of Sec. III B are shown in Fig. 6. The constructive interference of $|U_1|$ and $|U_2|$ is evident in Figs. 6(a) and 6(b). The time-dependent ratio $|U_1/U_2|$ plotted in Fig. 6(c) shows an oscillation with a period ~500 fs. The oscillation has a period similar to the one observed

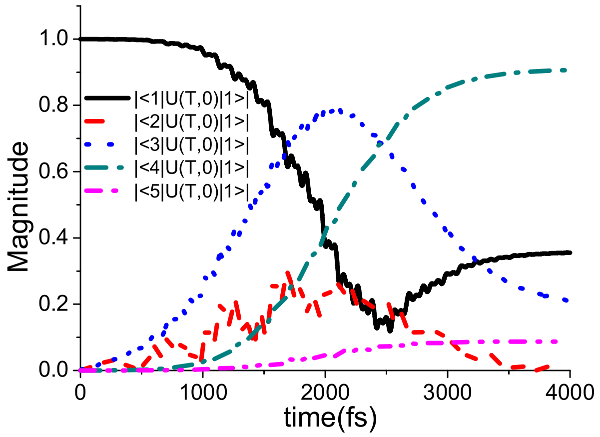

FIG. 4. (Color online) The control field driven dynamics for the magnitude of the amplitudes for all five states of atomic Rb expressed as $|\langle j|U(T,0)|1\rangle|$, $j = 1,\ldots,5$. The population of a state is the square of its amplitude. The control field is optimized with amplitudes A_k in Eq. (12) being limited in the range [0, 4.0×10^{-5}]. In this case, the second pathway in Fig. 1 is dominant.

TABLE III. The distribution of significant pathway orders for the control field driven dynamics in Fig. 4.

Order	Amplitude	Phase
2	1.9698	0.6779
4	1.3967	−2.3518
6	0.3782	0.9754
8	0.05121	−1.8258

TABLE IV. Amplitudes and phases of significant 2nd- and 4th-order quantum pathways for the control field driven dynamics in Fig. 4.

Pathway	Amplitude	Phase
$(1 \to 3 \to 4)$ (Pathway 2)	1.7631	0.6946
$(1 \to 2 \to 4)$ (Pathway 1)	0.2091	0.5369
$(1 \to 3 \to 1 \to 3 \to 4)$	0.7591	−2.4606
$(1 \to 3 \to 4 \to 3 \to 4)$	0.3542	−2.4417
$(1 \to 2 \to 1 \to 3 \to 4)$	0.2083	−1.2613
$(1 \to 3 \to 1 \to 2 \to 4)$	0.09128	−2.7247
$(1 \to 3 \to 4 \to 2 \to 4)$	0.04999	−2.6620
$(1 \to 2 \to 4 \to 3 \to 4)$	0.04359	−2.5987
$(1 \to 2 \to 1 \to 2 \to 4)$	0.01095	2.9914

experimentally [29], which indicates that the mechanism discussed here may have also contributed to the laboratory findings even though the laboratory field was qualitatively different (i.e., the experiments in Ref. [29] used broadband laser pulses). When pathway 2 dominates in the dynamics (see the second case discussed in Sec. III B) this oscillation feature in $|U_1/U_2|$ disappears as shown in Fig. 6(d).

The analysis below shows that for the low-bandwidth pulses considered here, the time-dependent amplitude ratio of the two pathways has a simple analytical form which enables the identification of the physical origin of the oscillations. For simplicity, a rectangular pulse is adopted in the analysis,

$$\begin{aligned} E(t) &= \sum_{k=1}^{4} A_k \cos(\omega_k t + \varphi_k) \\ &= \frac{1}{2}\sum_{k=1}^{4}(A_k e^{i(\omega_k t+\varphi_k)} + \text{c.c.}), \quad t \geqslant 0. \end{aligned} \tag{18}$$

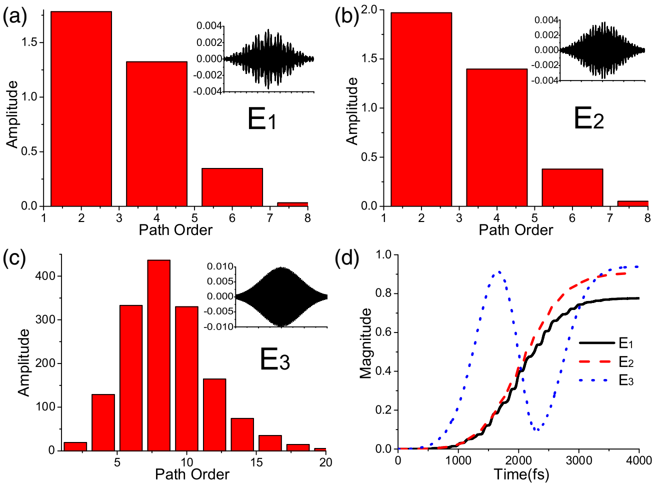

FIG. 5. (Color online) (a)–(c) The pathway order distribution $|U_{41}^n|$ for different laser fields. (d) The control field driven dynamics for the magnitude of the amplitudes for state $|4\rangle$ of atomic Rb expressed as $|\langle 4|U(T,0)|1\rangle|$ at different laser fields. E_1 and E_2 correspond to the cases in Sec. III B. The inset figures in (a)–(c) show that the laser field amplitude increases from E_1 to E_3.

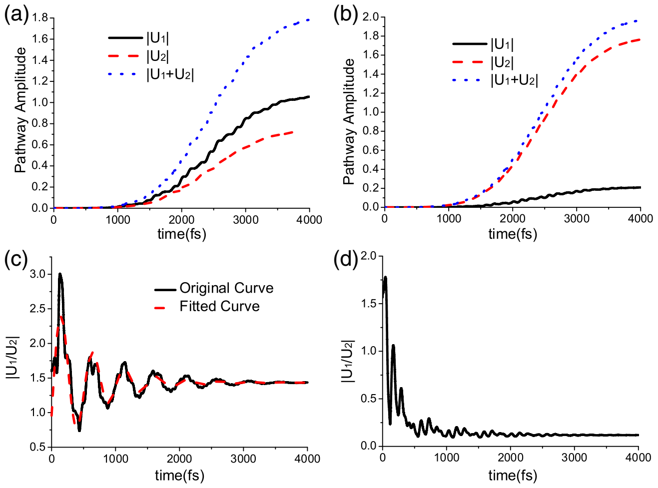

FIG. 6. (Color online) (a), (b) The absolute value $|U_1(t)|$, $|U_2(t)|$, and $|U_1(t)+U_2(t)|$ for E_1 and E_2, respectively. There is evident constructive interference between U_1 and U_2 consistent with their very similar phases in Tables II and IV. (c), (d) The pathway amplitude ratio $|U_1(t)/U_2(t)|$ for E_1 and E_2, respectively. In (c), the $|U_1(t)/U_2(t)|$ curve (black solid line) for E_1 is fitted with a simple function (red dashed line) discussed in Sec. IV. The control fields E_1 and E_2 are optimized with amplitudes A_k in Eq. (14) being limited in the ranges $[0, 2.5 \times 10^{-5}]$ and $[0, 4.0 \times 10^{-5}]$, respectively.

The pathway amplitudes $|U_1|$ and $|U_2|$ correspond to two Dyson terms in Eqs. (15) and (16).

In the rotating-wave approximation [32], we have

$$\begin{aligned} U_1 &= \frac{\mu_{12}\mu_{24}}{4}\sum_{p,q}^{4}\int_0^t e^{-i\omega_3 t_2} A_q e^{i(\omega_q t_2+\varphi_q)} \\ &\quad \times \int_0^{t_2} e^{-i\omega_1 t_1} A_p e^{i(\omega_p t_1+\varphi_p)} dt_1 dt_2 \\ &= \frac{\mu_{12}\mu_{24}}{4}\sum_{p,q}^{4} A_p A_q V_{pq}^{(13)}(t) \end{aligned} \tag{19}$$

and

$$\begin{aligned} U_2 &= \frac{\mu_{13}\mu_{34}}{4}\sum_{p,q}^{4}\int_0^t e^{-i\omega_4 t_2} A_q e^{i(\omega_q t_2+\varphi_q)} \\ &\quad \times \int_0^{t_2} e^{-i\omega_2 t_1} A_p e^{i(\omega_p t_1+\varphi_p)} dt_1 dt_2 \\ &= \frac{\mu_{13}\mu_{34}}{4}\sum_{p,q}^{4} A_p A_q V_{pq}^{(24)}(t) \end{aligned} \tag{20}$$

with

$$V_{pq}^{(mn)}(t) = \int_0^t e^{-i\omega_n t_2} e^{i(\omega_q t_2+\varphi_q)} \int_0^{t_2} e^{-i\omega_m t_1} e^{i(\omega_p t_1+\varphi_p)}. \tag{21}$$

It is easy to see that the resonant terms are $V_{13}^{(13)}$ and $V_{24}^{(24)}$ for U_1 and U_2, respectively, while all other terms are nonresonant. The analytical formulas of $V_{pq}^{(mn)}$ are displayed in the Appendix. The magnitudes of the nonresonant terms are determined by the detunings which are listed in Table V. It

TABLE V. The detunings between the four frequencies. The values are given according to the relation $\Delta\omega_{ij} = \omega_i - \omega_j$. The smallest detuning among nonresonant transitions is $\Delta\omega_{31} = -\Delta\omega_{13} = 30.7 \times 10^{-5}$ a.u.

Detuning (10^{-5} a.u.)	ω_1	ω_2	ω_3	ω_4
ω_1	0	108.26	−30.7	−138.96
ω_2	−108.26	0	−138.96	−247.22
ω_3	30.7	138.96	0	−108.26
ω_4	138.96	247.22	108.26	0

can be verified that the largest nonresonant terms for pathway 1 are $V_{11}^{(13)}$, $V_{33}^{(13)}$, and $V_{31}^{(13)}$, and the largest nonresonant terms for pathway 2 are $V_{13}^{(24)}$, $V_{23}^{(24)}$, and $V_{14}^{(24)}$. From the values of the $V_{pq}^{(mn)}$ given in the Appendix, it can be shown that

$$\begin{aligned} &\left|V_{13}^{(13)}(t)\right| = \left|V_{24}^{(24)}(t)\right| \\ &\gg \left|V_{11}^{(13)}(t)\right| = \left|V_{33}^{(13)}(t)\right| = \left|V_{31}^{(13)}(t)\right| \\ &\gg \left|V_{13}^{(24)}(t)\right| = \left|V_{23}^{(24)}(t)\right| = \left|V_{14}^{(24)}(t)\right|. \end{aligned} \tag{22}$$

Keeping the resonant terms and the largest nonresonant terms yields a simple equation for the pathway ratio:

$$\begin{aligned} \frac{U_1}{U_2} &\approx \frac{A_1A_3V_{13}^{(13)} + A_1A_1V_{11}^{(13)} + A_3A_3V_{33}^{(13)} + A_3A_1V_{31}^{(13)}}{A_2A_4V_{24}^{(24)} + A_1A_3V_{13}^{(24)} + A_2A_3V_{23}^{(24)} + A_1A_4V_{14}^{(24)}} \\ &\quad\times \frac{\mu_{12}\mu_{24}}{\mu_{13}\mu_{34}} \\ &\approx \frac{A_1A_3V_{13}^{(13)} + A_1A_1V_{11}^{(13)} + A_3A_3V_{33}^{(13)} + A_3A_1V_{31}^{(13)}}{A_2A_4V_{24}^{(24)}} \\ &\quad\times \frac{\mu_{12}\mu_{24}}{\mu_{13}\mu_{34}} \\ &\approx \frac{V_{13}^{(13)}}{V_{24}^{(24)}} \frac{A_1A_3\mu_{12}\mu_{24}}{A_2A_4\mu_{13}\mu_{34}} \\ &\quad + \frac{A_1A_1V_{11}^{(13)} + A_3A_3V_{33}^{(13)} + A_3A_1V_{31}^{(13)}}{A_2A_4V_{24}^{(24)}} \frac{\mu_{12}\mu_{24}}{\mu_{13}\mu_{34}}. \end{aligned} \tag{23}$$

Here the first term is time independent, but the second term oscillates with time. The detuning $|\Delta\omega_{31}| = |\Delta\omega_{13}| = 30.7 \times 10^{-5}$ a.u. in the second term corresponds to an oscillation with a 495 fs period. Taking a simple case as an illustration, we set all of the control field phases to be π and all of amplitudes in the control field to be the same; then the ratio becomes

$$\begin{aligned} \frac{U_1(t)}{U_2(t)} &\approx \left[1 + \frac{2}{\Delta\omega_{31}^2 t^2}\left(1 - e^{it\Delta\omega_{31}} + e^{-it\Delta\omega_{31}}\, it\Delta\omega_{31}\right)\right] \\ &\quad\times \frac{\mu_{12}\mu_{24}}{\mu_{13}\mu_{34}}. \end{aligned} \tag{24}$$

It can be easily seen that the detuning ($\Delta\omega_{31}$) between the transitions $5S_{1/2} \rightarrow 5P_{3/2}$ (ω_1) and $5P_{3/2} \rightarrow 5D_{3/2}$ (ω_3) induces the oscillation of $|U_1/U_2|$.

Although the laser field adopted in the analysis above does not have the Gaussian envelope employed in the simulations of Sec. III, the conclusion drawn about the temporal oscillation from the simpler field here should still be qualitatively valid for $E(t)$ given in Eq. (14). This conclusion is confirmed by the excellent fitting of the $|U_1/U_2|$ curve in Fig. 6 with the function

$$f(t) = a - b\,\exp(-ct)\,\sin(\Delta\omega_{31}t + \phi). \tag{25}$$

Least squares was used to fit the curve with the parameters $a = 1.434\,63$, $b = 1.248\,47$, $c = 3.901\,56 \times 10^{-5}$, and $\phi = 2.748\,67$. The fitting function shows that the oscillation has a period of $2\pi/\Delta\omega_{31}$. According to Eq. (23), the value of the constant a should be

$$\begin{aligned} \frac{A_1A_3\mu_{12}\mu_{24}}{A_2A_4\mu_{13}\mu_{34}} &= \frac{1.0544 \times 2.4860 \times 4.2275 \times 1.0216}{1.1691 \times 2.4833 \times 2.9931 \times 0.9} \\ &= 1.448. \end{aligned}$$

This value is very close to the fitted value of 1.435, and the overall behavior is consistent with the oscillation arising from the frequency difference between $5S_{1/2} \rightarrow 5P_{3/2}$ and $5P_{3/2} \rightarrow 5D_{3/2}$ transitions.

V. CONCLUDING REMARKS

We used HE-OD to study the pathway dynamics in the optimal quantum control of atomic Rb with the five-level model in Fig. 1. Population can be driven from the initial state to the target state through pathway 1, $5S_{1/2} \rightarrow 5P_{3/2} \rightarrow 5D_{3/2}$, or pathway 2, $5S_{1/2} \rightarrow 5P_{1/2} \rightarrow 5D_{3/2}$, which constitute the two lowest order routes for reaching $5D_{3/2}$. These two pathways present an interesting dynamical situation. The intermediate state $5P_{3/2}$ of pathway 1 is coupled to both the target state $5D_{3/2}$ and the additional state $5D_{5/2}$. Thus, pathway 1 leads to an undesired "leakage." Nevertheless, the transition dipoles of pathway 1 are larger, which somewhat balances the leakage effect. On the other hand, the intermediate state $5P_{1/2}$ of pathway 2 can only be excited to the target state. The competition between the two pathways will be determined by the balance of the factors above and also the freedom available in the field to manage the dynamics. Three cases were analyzed using HE-OD. In case 1, the four amplitude parameters are constrained to a small value, and only the second- and fourth-order pathways have significant contributions and cooperate with each other to achieve the task. In case 2, the four amplitude parameters are constrained to a higher range such that the pulse drives most of the population to the target state through pathway 2 in order to avoid losing population to the undesired state. The laser fields for these two cases have modest peak amplitude. In case 3, the control field is much stronger, and higher than fourth-order pathways become dominant. We also obtain an analytical explanation regarding the oscillation of the ratio of the two pathway amplitudes. A simple analytical model shows that the frequency of the oscillation may be determined by the frequency difference between the $5S_{1/2} \rightarrow 5P_{3/2}$ and $5P_{3/2} \rightarrow 5D_{3/2}$ transitions.

The theoretical analysis here illustrates the use of HE-OD for finding quantum control mechanisms. HE-OD is a broadly applicable input-output modulation tool, which can be flexibly applied in a variety of circumstances. For example, under modulation, the intrinsic properties of the system will result in particular signatures in the output, which may be employed to identify key system characteristics (i.e., error identification for quantum devices). Our analysis gives a quantitative relationship between the oscillation behavior (i.e., the oscillation period and average value of $|U_1/U_2|$) and the system Hamiltonian, which illustrates the possible use of HE-OD for Hamiltonian identification. Since extracting the quantum mechanism also allows for its manipulation [28], HE-OD guided experiments may be used for steering about quantum dynamics. This capability may be applied in quantum state preparation or possibly to avoid chemical reaction bottlenecks, etc. The laser fields used in this work differ from the laboratory fields used in Refs. [28,29] in that the laboratory fields had a much larger bandwidth possibly leading to more complex mechanisms. Nevertheless, the model considered here provides a reasonable physical picture. Planned further developments of HE-OD include the treatment of open quantum systems, which may allow for the study of decoherence processes.

ACKNOWLEDGMENTS

This work is supported by National Natural Science Foundation of China (Grants No. 61074052, No. 61203061, and No. 61374091). H.R. acknowledges support from the Chinese Academy of Sciences Visiting Professorship for Senior International Scientists, and additional support from the US NSF (Grant No. CHE-1058644).

APPENDIX: RESONANT AND NONRESONANT DECOMPOSITION OF THE TWO DYSON TERMS

Consider a field of the form $E(t) = \sum_{k=1}^{4} A_k \cos(\omega_k t + \varphi_k)$. In the RWA approximation, the resonant term of U_1 at t is

$$V_{13}^{(13)} = \tfrac{1}{2} e^{i(\varphi_1+\varphi_3)} t^2. \tag{A1}$$

The largest non-resonant terms are

$$V_{11}^{(13)} = \frac{e^{2i\varphi_1} e^{it(\omega_1-\omega_3)}\{[1 - it(\omega_1-\omega_3)] - e^{-it(\omega_1-\omega_3)}\}}{(\omega_1-\omega_3)^2}, \tag{A2}$$

$$V_{33}^{(13)} = \frac{e^{2i\varphi_3}\{[1 - it(\omega_1-\omega_3)] - e^{-it(\omega_1-\omega_3)}\}}{(\omega_1-\omega_3)^2}, \tag{A3}$$

$$V_{31}^{(13)} = \frac{e^{i(\varphi_1+\varphi_3)}\{[1 + it(\omega_1-\omega_3)] - e^{it(\omega_1-\omega_3)}\}}{(\omega_1-\omega_3)^2}. \tag{A4}$$

The other nonresonant terms are w

$$V_{21}^{(13)} = \frac{e^{i(\varphi_1+\varphi_2)}}{-\omega_1+\omega_2}\left(\frac{-1 + e^{it(\omega_1-\omega_3)}}{\omega_1-\omega_3} - \frac{-1 + e^{it(\omega_2-\omega_3)}}{\omega_2-\omega_3}\right), \tag{A5}$$

$$\begin{aligned} V_{41}^{(13)} = {} & \frac{e^{-i(t\omega_3-\varphi_1-\varphi_4)}}{(\omega_1-\omega_3)(\omega_1-\omega_4)(\omega_3-\omega_4)}[e^{it\omega_4}(-\omega_1+\omega_3) \\ & + e^{it\omega_3}(\omega_1-\omega_4) + e^{it\omega_1}(-\omega_3+\omega_4)], \end{aligned} \tag{A6}$$

$$V_{12}^{(13)} = \frac{e^{i(\varphi_1+\varphi_2)}\{-1 + e^{it(\omega_2-\omega_3)}[1 - it(\omega_2-\omega_3)]\}}{(\omega_2-\omega_3)^2}, \tag{A7}$$

$$\begin{aligned} V_{22}^{(13)} = {} & \frac{e^{-it(\omega_1-2\omega_2+\omega_3)+2i\varphi_2}}{(\omega_1-\omega_2)(\omega_2-\omega_3)(\omega_1-2\omega_2+\omega_3)} \\ & \times [e^{it(\omega_1-2\omega_2+\omega_3)}(\omega_1-\omega_2) - \omega_2 + \omega_3 \\ & - e^{it(\omega_1-\omega_2)}(\omega_1-2\omega_2+\omega_3)], \end{aligned} \tag{A8}$$

$$\begin{aligned} V_{32}^{(13)} = {} & \frac{e^{-i(T\omega_1-\varphi_2-\varphi_3)}}{(\omega_1-\omega_2)(\omega_1-\omega_3)(\omega_2-\omega_3)} \\ & \times [e^{it(\omega_1+\omega_2-\omega_3)}(-\omega_1+\omega_2) \\ & + e^{it\omega_1}(\omega_1-\omega_3) + e^{it\omega_2}(-\omega_2+\omega_3)], \end{aligned} \tag{A9}$$

$$V_{42}^{(13)} = \frac{e^{i(\varphi_2+\varphi_4)}}{\omega_1-\omega_4}\left(\frac{1 - e^{it(\omega_2-\omega_3)}}{\omega_2-\omega_3} + it\right), \tag{A10}$$

$$V_{23}^{(13)} = \frac{e^{-i(t\omega_1-\varphi_2-\varphi_3)}\{-e^{it\omega_2} + e^{it\omega_1}[1 - it(\omega_1-\omega_2)]\}}{(\omega_1-\omega_2)^2}, \tag{A11}$$

$$V_{43}^{(13)} = \frac{e^{-i(t\omega_1-\varphi_3-\varphi_4)}\{-e^{it\omega_4} + e^{iT\omega_1}[1 - it(\omega_1-\omega_4)]\}}{(\omega_1-\omega_4)^2}, \tag{A12}$$

$$V_{14}^{(13)} = \frac{e^{-i[t(\omega_3-\omega_4)-\varphi_1-\varphi_4]}[1 - e^{it(\omega_3-\omega_4)} + it(\omega_3-\omega_4)]}{(\omega_3-\omega_4)^2}, \tag{A13}$$

$$V_{24}^{(13)} = \frac{e^{i(\varphi_2+\varphi_4)}}{\omega_1-\omega_2}\left(\frac{1 - e^{it(\omega_4-\omega_3)}}{\omega_4-\omega_3} + it\right), \tag{A14}$$

$$\begin{aligned} V_{34}^{(13)} = {} & \frac{e^{-i[t(\omega_1+\omega_3)-\varphi_3-\varphi_4]}}{(\omega_1-\omega_3)(\omega_1-\omega_4)(-\omega_3+\omega_4)} \\ & \times [e^{it(\omega_1+\omega_3)}(\omega_1-\omega_3) + e^{it(\omega_3+\omega_4)}(\omega_3-\omega_4) \\ & + e^{it(\omega_1+\omega_4)}(-\omega_1+\omega_4)], \end{aligned} \tag{A15}$$

$$\begin{aligned} V_{44}^{(13)} = e^{2i\varphi_4}\Bigg(& \frac{1 - e^{-it(\omega_1+\omega_3-2\omega_4)}}{(\omega_1+\omega_3-2\omega_4)(\omega_1-\omega_4)} \\ & + \frac{1 - e^{-it(\omega_3-\omega_4)}}{(\omega_3-\omega_4)(-\omega_1+\omega_4)}\Bigg). \end{aligned} \tag{A16}$$

In the same way, the resonant term of U_2 can be derived as

$$V_{24}^{(24)} = \tfrac{1}{2} e^{i(\varphi_2+\varphi_4)} t^2. \tag{A17}$$

The largest nonresonant terms are

$$V_{13}^{(24)} = \frac{e^{i(\varphi_1+\varphi_3)}\{[1 - it(\omega_1-\omega_2)] - e^{-it(\omega_1-\omega_2)}\}}{(\omega_1-\omega_2)^2}, \tag{A18}$$

$$V_{23}^{(24)} = \frac{e^{i(\varphi_2+\varphi_3)} e^{-it(\omega_1-\omega_2)}\{[1 + it(\omega_1-\omega_2)] - e^{it(\omega_1-\omega_2)}\}}{(\omega_1-\omega_2)^2}, \tag{A19}$$

$$V_{14}^{(24)} = \frac{e^{i(\varphi_1+\varphi_4)}\{[1 + it(\omega_1-\omega_2)] - e^{it(\omega_1-\omega_2)}\}}{(\omega_1-\omega_2)^2}. \tag{A20}$$

The other nonresonant terms are

$$V_{11}^{(24)} = \frac{e^{2i\varphi_1}}{\omega_1 - \omega_2}\left(\frac{-1 + e^{it(\omega_1 - \omega_4)}}{\omega_1 - \omega_4} + \frac{-1 + e^{it(2\omega_1 - \omega_2 - \omega_4)}}{-2\omega_1 + \omega_2 + \omega_4}\right), \tag{A21}$$

$$V_{21}^{(24)} = \frac{e^{i(\varphi_1 + \varphi_2)}\{-1 + e^{it(\omega_1 - \omega_4)}[1 - it(\omega_1 - \omega_4)]\}}{(\omega_1 - \omega_4)^2}, \tag{A22}$$

$$V_{31}^{(24)} = \frac{e^{i(\varphi_1 + \varphi_3)}}{\omega_3 - \omega_2}\left(\frac{-1 + e^{it(\omega_1 - \omega_4)}}{\omega_1 - \omega_4} - it\right), \tag{A23}$$

$$\begin{aligned} V_{41}^{(24)} = {} & \frac{e^{i(\varphi_1 + \varphi_4)}}{(\omega_1 - \omega_2)(\omega_1 - \omega_4)(\omega_2 - \omega_4)} \\ & \times [-\omega_2 + e^{it(\omega_1 - \omega_4)}(-\omega_1 + \omega_2) \\ & + e^{it(\omega_1 - \omega_2)}(\omega_1 - \omega_4) + \omega_4], \end{aligned} \tag{A24}$$

$$V_{12}^{(24)} = \frac{e^{i(\varphi_1 + \varphi_2)}}{-\omega_1 + \omega_2}\left(\frac{-1 + e^{it(\omega_1 - \omega_4)}}{\omega_1 - \omega_4} + \frac{1 - e^{it(\omega_2 - \omega_4)}}{\omega_2 - \omega_4}\right), \tag{A25}$$

$$V_{22}^{(24)} = \frac{e^{2i\varphi_2}\{-1 + e^{it(\omega_2 - \omega_4)}[1 - it(\omega_2 - \omega_4)]\}}{(\omega_2 - \omega_4)^2}, \tag{A26}$$

$$V_{32}^{(24)} = \frac{e^{i(\varphi_2 + \varphi_3)}}{-\omega_2 + \omega_3}\left(\frac{-1 + e^{it(\omega_2 - \omega_4)}}{\omega_2 - \omega_4} + \frac{1 - e^{it(\omega_3 - \omega_4)}}{\omega_3 - \omega_4}\right), \tag{A27}$$

$$V_{42}^{(24)} = \frac{e^{i(\varphi_2 + \varphi_4)}[1 - e^{it(\omega_2 - \omega_4)} + it(\omega_2 - \omega_4)]}{(\omega_2 - \omega_4)^2}, \tag{A28}$$

$$\begin{aligned} V_{33}^{(24)} = {} & \frac{e^{-it(\omega_2 - 2\omega_3 + \omega_4) + 2i\varphi_3}}{(\omega_2 - \omega_3)(\omega_3 - \omega_4)(\omega_2 - 2\omega_3 + \omega_4)} \\ & \times [e^{it(\omega_2 - 2\omega_3 + \omega_4)}(\omega_2 - \omega_3) - \omega_3 + \omega_4 \\ & - e^{it(\omega_2 - \omega_3)}(\omega_2 - 2\omega_3 + \omega_4)], \end{aligned} \tag{A29}$$

$$\begin{aligned} V_{43}^{(24)} = {} & \frac{e^{-i(t\omega_2 - \varphi_3 - \varphi_4)}}{(\omega_2 - \omega_3)(\omega_2 - \omega_4)(\omega_3 - \omega_4)}[e^{it(\omega_2 + \omega_3 - \omega_4)}(-\omega_2 + \omega_3) \\ & + e^{it\omega_2}(\omega_2 - \omega_4) + e^{it\omega_3}(-\omega_3 + \omega_4)], \end{aligned} \tag{A30}$$

$$V_{34}^{(24)} = \frac{e^{-i(t\omega_2 - \varphi_3 - \varphi_4)}\{-e^{it\omega_3} + e^{it\omega_2}[1 - it(\omega_2 - \omega_3)]\}}{(\omega_2 - \omega_3)^2}, \tag{A31}$$

$$V_{44}^{(24)} = \frac{e^{2i\varphi_4}[1 - e^{-it(\omega_2 - \omega_4)} - it(\omega_2 - \omega_4)]}{(\omega_2 - \omega_4)^2}. \tag{A32}$$

---

[1] C. Brif, R. Chakrabarti, and H. Rabitz, New J. Phys. **12**, 075008 (2010).

[2] J. M. Geremia, J. K. Stockton, and H. Mabuchi, Science **304**, 270 (2004).

[3] H. M. Wiseman and A. C. Doherty, Phys. Rev. Lett. **94**, 070405 (2005).

[4] H. Rabitz, R. de Vivie-Riedle, M. Motzkus, and K. Kompa, Science **288**, 824 (2000).

[5] J. Combes and K. Jacobs, Phys. Rev. Lett. **96**, 010504 (2006).

[6] G. G. Gillett, R. B. Dalton, B. P. Lanyon, M. P. Almeida, M. Barbieri, G. J. Pryde, J. L. O'Brien, K. J. Resch, S. D. Bartlett, and A. G. White, Phys. Rev. Lett. **104**, 080503 (2010).

[7] N. Yamamoto, H. I. Nurdin, M. R. James, and I. R. Petersen, Phys. Rev. A **78**, 042339 (2008).

[8] S. Mancini and H. M. Wiseman, Phys. Rev. A **75**, 012330 (2007).

[9] J. Zhang, Y.-X. Liu, R.-B. Wu, C.-W. Li, and T.-J. Tarn, Phys. Rev. A **82**, 022101 (2010).

[10] J. Zhang, Y.-X. Liu, and F. Nori, Phys. Rev. A **79**, 052102 (2009).

[11] J. Zhang, R.-B. Wu, C.-W. Li, and T.-J. Tarn, IEEE Trans. Autom. Control **55**, 619 (2010).

[12] R. S. Judson and H. Rabitz, Phys. Rev. Lett. **68**, 1500 (1992).

[13] C. Daniel *et al.*, Chem. Phys. **267**, 247 (2001).

[14] M. Roth, L. Guyon, J. Roslund, V. Boutou, F. Courvoisier, J. P. Wolf, and H. Rabitz, Phys. Rev. Lett. **102**, 253001 (2009).

[15] T. Brixner and G. Gerber, Chem. Phys. Chem. **4**, 418 (2003).

[16] R. Bartels *et al.*, Nature (London) **406**, 164 (2000).

[17] T. Feurer, J. Vaughan, and K. Nelson, Science **299**, 374 (2003).

[18] M. Aeschlimann *et al.*, Nature (London) **446**, 301 (2007).

[19] T. Weinacht, J. Ahn, and P. Bucksbaum, Nature (London) **397**, 233 (1999).

[20] J. Petersen, R. Mitrić, V. Bonačić-Koutecký, J.-P. Wolf, J. Roslund, and H. Rabitz, Phys. Rev. Lett. **105**, 073003 (2010).

[21] T. Brixner, B. Kiefer, and G. Gerber, Chem. Phys. **267**, 241 (2001).

[22] A. Mitra, I. R. Solá, and H. Rabitz, Phys. Rev. A **67**, 043409 (2003).

[23] A. Mitra, I. R. Solá, and H. Rabitz, Phys. Rev. A **77**, 043415 (2008).

[24] A. Mitra and H. Rabitz, Phys. Rev. A **67**, 033407 (2003).

[25] A. Mitra and H. Rabitz, J. Chem. Phys. **125**, 194107 (2006).

[26] A. Mitra and H. Rabitz, J. Chem. Phys. **128**, 044112 (2008).

[27] R. Rey-de-Castro and H. Rabitz, Phys. Rev. A **81**, 063422 (2010).

[28] R. Rey-de-Castro, Z. Leghtas, and H. Rabitz, Phys. Rev. Lett. **110**, 223601 (2013).

[29] R. Rey-de-Castro, R. Cabrera, D. I. Bonder, and H. Rabitz, New J. Phys. **15**, 025032 (2013).

[30] S. B. Bayram, M. Havey, M. Rosu, A. Sieradzan, A. Derevianko, and W. R. Johnson, Phys. Rev. A **61**, 050502 (2000).

[31] Data of the energy levels and transition dipoles can be found at the website http://www.steck.us/alkalidata/rubidium85numbers.pdf.

[32] I. I. Rabi, N. F. Ramsey, and J. Schwinger, Rev. Mod. Phys. **26**, 167 (1954).